Two-node curved inverse finite element formulations based on exact strain-displacement solution

J. Appl. Comput. Mech., xx(x) (2023) 1-15
DOI: 10.22055/jacm.2022.41150.3708

ISSN: 2383-4536
jacm.scu.ac.ir

Shahid Chamran University of Ahvaz

Journal of Applied and Computational Mechanics

Research Paper

Two-node Curved Inverse Finite Element Formulations based on Exact Strain-displacement Solution

Pierclaudio Savino[1], Francesco Tondolo[2]

[1] Department of Structural, Geotechnical and Building Engineering, Politecnico di Torino, Turin, 10129, Italy, Email: pierclaudio.savino@polito.it

[2] Department of Structural, Geotechnical and Building Engineering, Politecnico di Torino, Turin, 10129, Italy, Email: francesco.tondolo@polito.it

Received June 20 2022; Revised August 25 2022; Accepted for publication August 26 2022.
Corresponding author: P. Savino (pierclaudio.savino@polito.it)

Abstract. The inverse finite element method (iFEM) is an efficient algorithm developed for real-time monitoring of structures equipped by a network of strain sensors. The inverse element for modeling curved beams was previously developed using an approximate solution based on independently interpolated displacement components. In this study, a new formulation is proposed by the development of a least-squares variational principle using the kinematic framework of the curved beam theory. The library of existing iFEM-based elements is expanded by introducing three different inverse curved elements named iCB3, iCB4 and iCB5 respectively. This new formulation has been developed considering the exact solution of the curved beam theory that corresponds to the membrane-bending coupling and the explicit statement of the rigid-body motions. The three inverse elements, which require three, four and five measurement points respectively, extend the practical utility of iFEM for shape sensing analysis of curved structures according to the minimum available quantity of strain sensors. The effectiveness and higher accuracy of the iCB/iFEM methodology compared to other solutions present in literature are demonstrated considering numerical studies on curved beams under static transverse force and distributed loading conditions. For these problems, the effect of strain measurements error, number of sensors and discretization refinement on the solution accuracy is evaluated.

Keywords: Shape sensing, inverse finite element method, structural health monitoring, curved beam, strain sensors.

1. Introduction

All structures belonging to different engineering fields share a common problem represented by structural decay. Apart from the specific origin, these are subjected to increasingly harsh environment, cyclic or extreme loadings, corrosion, which lead to challenging operating conditions. As a consequence, structural failures may occur more frequently, maintenance costs become very expensive and the safety levels are reduced. Therefore, for a better management of structural and infrastructural assets it is critical the knowledge of structural integrity and improve on-site assessment of structural performance. A procedure to obtain real-time information on the structural state, unusual structural behaviours and unhealthy structural conditions is known as structural health monitoring (SHM). The development of an efficient and reliable integrated SHM system allows to increase human and structural safety, decreases maintenance costs and reduces service downtime considering optimal periods for inspection and repairs. A promising technology for SHM procedure that processes data collected from the on-board sensors in real-time is known as shape and stress sensing. Processing the data collected by a network of strain sensors, it is possible to reconstruct the deformed shape and stress fields of a structure, allowing the damage prediction by means of a proper failure criterion and evaluate residual safety.

A powerful mechanics-based algorithm called inverse Finite Element Method (iFEM) was developed by Tessler and Spangler [1, 2] at NASA Langley Research Centre, for real-time shape sensing of aerospace vehicles. The theoretical framework is based on a least-squares variational principle that allows the reconstruction of the full-field displacements from measured surface strains of shear-deformable plate and shell structures. The error functional matches in the least-squares sense the analytical strains, explained in terms of C0 continuous displacement interpolation functions, and measured strains. Since the methodology involves only strain-displacements relations, the structural deformed shapes can be reconstructed without any knowledge of elastic or inertial material properties. Once the full-field displacements are obtained, the full-field strains and stress state can be evaluated by referring to the material properties of the structure. Involving the stresses in a proper failure criterion a real-time damage prediction can be enabled.

The iFEM approach has been extensively studied over the past fifteen years, including the development of various types of inverse elements and theoretical framework. The formulation has been extended by Gherlone [3] to reconstruct the complete displacements field for beam and frame structures according to Timoshenko beam theory, which includes the axial, bending, torsion and transverse shear deformations. Gherlone et al. [4, 5] proposed two inverse finite elements for the Timoshenko beams whose

Published online: September 08 2022

order of kinematic interpolations is related to the number of required strain gauges. The solution accuracy is examined with respect to the numerical simulation of a thin-walled cantilevered beam subjected to harmonic excitations in the presence of structural damping. To reconstruct the deformed shape of multi-layered composite and sandwich structures possessing a high degree of anisotropy and heterogeneity, Cerracchio et al. [6] introduced the kinematic assumptions of the Refined Zigzag Theory (RZT) into the iFEM framework. A new four-node inverse quadrilateral shell element (iQS4) was introduced by Kefal et al. [7], expanding the existing library of iFEM-based inverse elements. Numerical studies have been performed to verify the effectiveness of the quadratic interpolation functions adopted, to avoid singular solution in case of complex shell structures, membrane and shear locking phenomena. Kefal et al. [8] proposed an improved iFEM formulation to model laminated composite and sandwich plates and shells. The methodology involves the kinematics of RZT as a baseline for the development of a three-node inverse-shell element named i3-RZT. The linear incremental iFEM procedure has been introduced by Tessler et al. [9] to reconstruct the displacement field of a shell structure undergoing geometric nonlinearity. The procedure, involving at each load step the incremental strains, provides displacements which in turn update the new geometry of the deformed shape. A new eight-node curved inverse-shell element, named iCS8, was developed by Kefal [10] through combining the kinematics assumptions of both solid shell and first-order shear deformation plate theory. Savino et al. [11] proposed a new iFEM formulation according to the kinematics assumption of the Bernoulli-Euler theory. Two inverse beam finite elements have been formulated for a better optimization of the number of strain measurements required. Due to the impact given by the experimental error in the strain measurements which could decrease the quality of the displacement solutions, Kefal et al. [12] developed "smooted iFEM" method for performing shape and stress sensing applying smoothing of in situ strain measurements. Since iFEM analysis of curved structures modelled with existing flat inverse-shell elements requires more refined mesh generation and thus a large number of strain sensors, Kefal and Oterkus [13] expanded the iFEM methodology introducing a novel isogeometric inverse element. The isogeometric inverse-shell element, named iKLS, is based on membrane and bending strains consistent with the Kirchoff-Love shell theory. Savino et al. [14] developed a two-node inverse curved beam element based on quintic-degree polynomial shape functions to guarantee accurate reconstructions without the need to explicitly solve the governing differential equations for the strain-displacement problem. Moreover, the application of the inverse elements formulated not only involved the full-field structural deformed shape and stress-strain reconstruction but also the detection of possible damage locations. Colombo et al. [15, 16] used the iFEM algorithm to create a load-adaptive baseline for damage identification based on an anomaly index. Furthermore, they investigated the damage localization capability by comparing the trends in anomaly indices between the different sub-regions of the structures. The comparison of the strain computed by the iFEM and the strain measured by the test sensors provides the probability that the damage is close the test sensor. Roy et al. [17] investigated the use of the iFEM to localize damages by reconstructing the damaged strain field of the structure. Dividing the structure into square grid cells having strain sensors located at the boundaries, the iFEM reconstructs strain field with higher magnitude in those cells affected by damage. Li et al. [18] presented the application of iFEM approach to identify dent damage in a thin-walled cylindrical structures modelled with iQS4 element and representing the columns of floating offshore installations. In order to overcome potential constraints on sensor grid design given by the experimental setup, Oboe et al. [19] proposed a pre-extrapolation of the strain field by integrating the Smoothing Element Analysis algorithm within the iFEM framework. The minimization of the Penalized Discrete Least Square functional of the error between measured and numerical input strain field allows to compute the vector of the global degrees of freedom (DOF) from which interpolate the strain field on all desired locations. As a result, could be no limitation on the number of input sensors to obtain ever finer meshes and accurate results.

The mathematical concepts of the iFEM algorithm have been demonstrated with numerical and experimental application to SHM of aerospace, marine and mechanical structures. Quach et al. [20] combined fiber-optic strain sensing technology and iFEM to identify structural anomalies that may provide early indication of airframe structure degradation. The laboratory tests highlighted the effectiveness of the technique to detect anomalies as a trend of successively larger strain deviations from the no-damage state. The efficiency and predictive capability of the iFEM formulation have been investigated by Gherlone et al. [21] considering a laboratory experiment on a thin-walled cantilever beam subjected to various static loadings. The accuracy of the deformed shape reconstructed by strain-rosette data, has been assessed by comparing the iFEM outcomes with displacement transducers measurements. An application with experimentally measured strains according to the Timoshenko beam theory has been presented by Gherlone et al. [22], using both low-fidelity and high-fidelity discretization models. To verify the accuracy of the formulation, the iFEM predicted displacements are compared with those measured by the displacement transducers for static load cases or recovered by accelerometer for dynamic load cases. Kefal and Oterkus [23] performed displacement and stress monitoring of a typical chemical tanker mid-ship based on iFEM methodology. The effectiveness of the iQS4 inverse-shell element has been demonstrated by Kefal and Oterkus [24] for monitoring in case of multi-axial deformations and stresses considering a numerically simulated containership. Papa et al. [25] validated the iFEM formulation with the Mindlin plate approximation on a wing box extracted from total wing of an unmanned aircraft vehicle properly equipped with strain gages. Considering the iFEM-RZT methodology, Kefal and Yildiz [26] investigated the effect of sensor density and alignment on the shape sensing of a tapered wing-shaped sandwich panel subjected to bending, torsion and membrane loads. Zhao et al. [27] verified the iFEM approach based on the kinematics assumptions of Timoshenko beam theory through a simple supported beam and an experimental aluminum wing-like frame model. Since the deformation of the gantry structure in heavy-duty machine tools is an important factor that affects machining accuracy, Liu et al. [28, 29] verified the accuracy of the iFEM algorithm integrated with fiber Bragg grating sensors to realize real-time monitoring in the mechanical manufacturing field. Moreover, Liu et al. [30] demonstrated the application of the iFEM methodology also for monitoring the deformation of the column of heavy-duty machine tools. Zhao et al. [31, 32] constructed an optimal placement model of strain sensors based on eigenvalue analysis to monitor the wing frame deformation according to the iFEM algorithm based on Timoshenko theory. The optimal result of the multi-parameter optimization problem is provided by using the Particle Swarm Optimization algorithm. Kobayashi and Murayama [33] applied iFEM formulation to reconstruct buckling deformation of mode 1 and 2 of a simulated thin-wall pipe structure. Kefal et al. [34] applied the iQS4/iFEM methodology for real-time monitoring of 3D strains and stresses of a capsize bulk carrier. Niu et al. [35] presented a multi-nodes iFEM that reconstructs the displacement of a flexible antenna panel consistent with Mindlin plate theory; in order to clearly localize the damage, an additional damage parameter based on von Mises equivalent strain is introduced. Li et al. [36] applied iFEM analysis with iQS4 element, to monitor the tower of an offshore wind turbines under both static and dynamic loads.

The main focus of the current study is to expand the library of iFEM-based inverse curved elements and provide an enhanced iFEM formulation according to the exact solution of the governing differential equations for the curved beam problem. It is today widely recognized that to have good accuracy and convergence properties, it is important that the displacement field of a finite element (FE) incorporated an adequate representation of the rigid body motions (Dawe [37]). Previous iFEM-curved beam algorithm has been developed using independently interpolated displacement components which only approximate the rigid-body displacements. Moreover, the nodal DOF considered are compatible only for the simplified case of locally shallow arch, where the coupling between the membrane and bending behavior could be neglected. Considering the derivatives of the displacement components as nodal parameters and not the exact coupled terms, does not provide the true generalized strains. Since the rigid body displacements of finite elements with curved axis are expressed in trigonometric terms, the choice of independently

interpolating polynomial functions leads to nonconforming elements. The precise representation of rigid body motions requires the development of their explicit expression. On the other hand, to adequately represent strain-free motions, more DOF are often needed than a coupled displacement model (Dawe [38]). To address the aforementioned drawbacks, natural ("exact") shape functions are obtained by integrating the strain-displacements equations, which allow to calculate exactly the behavior of arches. Three types of such shape functions are developed, named iCB3, iCB4 and iCB5, having an increasing both accuracy and minimum number of strain sensors required. The main focus of the new inverse elements is to create accurate iFEM models with an iCB3-based coarse discretization using only three strain measurement points (station points) up to the most refined iCB5 considering five station points as minimum number. To consider higher degrees of the interpolant shape functions, the nodal continuities for both exact displacement and strain fields have been imposed. Validation problems are considered, including a semi-arch cantilever beam subjected to concentrated force and a fully clamped arch under distributed load. For these problems, different discretization refinements and the effects of strain measurements error on the accuracy of the iFEM solution are examined. To simulate the strain measurements and obtain the displacement reference solutions, direct FEM analyses are performed using LUSAS software (LUSAS [39]). Finally, the effects of sensors number and type of inverse element are assessed with respect to the solution accuracy for future practical applications of SHM systems.

2. Bernoulli-Euler Curved Beam Formulation

In the present paper, for the aforementioned purposes it has been considered a thin curved beam with constant cross-section and radius of curvature R, referred to the polar coordinate system (r, β) and curvilinear reference system (s, y, z) depicted in Fig. 1. The element is characterized by a Young's modulus E, moment of inertia Iz, cross-section area A and total length L. The present formulation is based on the following assumptions:

- small strains and displacements;
- homogeneous, isotropic and linear elastic material;
- beam axis always in the plane of bending;
- plane cross-section remains plane after loading.

Given the cross-section with assigned reference systems, the corresponding displacement field of the curved beam in curvilinear coordinates can be written as:

$$\begin{aligned} u_s(s,\, y,z) &= u(s) - y\varphi_z(s) \\ u_r(s,\, y,z) &= v(s) \\ u_z(s,\, y,z) &= 0 \end{aligned} \tag{1}$$

where u_s, u_r and u_z denote the displacements of the curved beam in the s, y and z directions respectively, u(s) and v(s) are the tangential and radial displacements of an arbitrary arch with length s measured on the neutral axis, and $\varphi_z(s)$ is the angle of rotation due to bending around the z axis. The kinematic variables that completely define the displacement field can be grouped in the vector:

$$\mathbf{u} = \{u,\, v,\, \varphi_z\}^T \tag{2}$$

As an assumption for straight beam in bending, all longitudinal fibers have the same length. Since curved beams are characterized by a significant initial curvature, the longitudinal fibers have different lengths and the linear variation of longitudinal strains over the cross-section is no longer valid, even if the assumption that plane cross section remain plane after deformation is still valid. This implies that in-plane normal strain is proportional to the distance of the fiber from the neutral axis which is no more coincident with the centroidal axis but is shifted towards the centre of curvature (Fig. 1). Considering a differential segment with subtended angle dβ (Fig. 2), the relation between the neutral axis (ds_n) with radius R_n and a general fiber (ds_i) at y_i distance from the neutral axis can be written as:

$$\frac{d}{ds_i} = \frac{d}{ds_n}\frac{ds_n}{ds_i} \tag{3}$$

where the length ds_n of the neutral axis fiber and ds_i of the generic fiber result:

$$\begin{aligned} ds_n &= R_n d\beta \\ ds_i &= (R_n + y_i)d\beta \end{aligned} \tag{4}$$

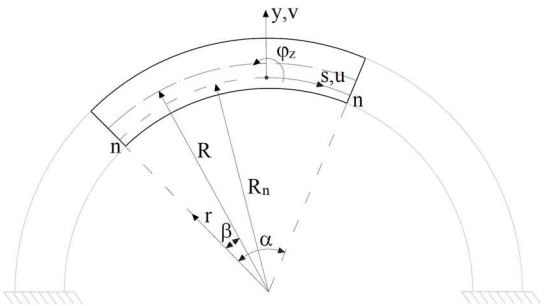

Fig. 1. Configuration of an arbitrary curved beam element.

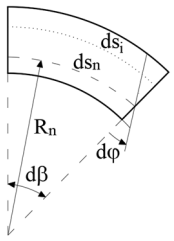

Fig. 2. Segment of curved beam with curvilinear axis.

Substituting Eq. 4 into Eq. 3 gives:

$$\frac{\mathrm{d}}{\mathrm{ds_i}} = \frac{\mathrm{R_n}}{(\mathrm{R_n} + \mathrm{y_i})} \frac{\mathrm{d}}{\mathrm{ds_n}} \tag{5}$$

where $\mathrm{d/ds_i}$ varies over the section with hyperbolic law. From Eq. 5, it can be assumed that the axial derivative of a generic fiber $\mathrm{s_i}$ can be computed with respect to the neutral axis $\mathrm{s_n}$, by taking into account the non-linear dependence along y.

Substituting Eq. 1 into the strain-displacement relations belonging to the Bernoulli-Euler theory, and considering the dependence given by Eq. 5, the consequent strain field is characterized by the normal strain written as (Qatu [40]):

$$\varepsilon_s(\mathrm{s},\ \mathrm{y},\mathrm{z}) = \frac{\mathrm{R_n}}{(\mathrm{R_n} + \mathrm{y})}\left[\varepsilon_0(\mathrm{s}) - \mathrm{y}\chi_0(\mathrm{s})\right] \tag{6}$$

where $\varepsilon_0(\mathrm{s})$ is the tangential strain and $\chi_0(\mathrm{s})$ the curvature. Since the tangential displacement u(s) gives a negative angular variation $\varphi_z(\mathrm{s})$, and the radial displacement v(s) leads to a positive axial strain $\varepsilon_0(\mathrm{s})$, the kinematics equations result:

$$\begin{aligned} \varepsilon_0(\mathrm{s}) &= \frac{\mathrm{du}}{\mathrm{ds}} + \frac{\mathrm{v}}{\mathrm{R}} \\ \chi_0(\mathrm{s}) &= \frac{\mathrm{d}\varphi_z}{\mathrm{ds}} = \frac{\mathrm{d}^2\mathrm{v}}{\mathrm{ds}^2} - \frac{1}{\mathrm{R}}\frac{\mathrm{du}}{\mathrm{ds}} \end{aligned} \tag{7}$$

The section strains that define the Bernoulli-Euler model can be written in the vector form:

$$\mathbf{e}(\mathbf{u}) = \begin{Bmatrix} \varepsilon_0 \\ \chi_0 \end{Bmatrix} = \begin{bmatrix} \frac{\mathrm{d}}{\mathrm{ds}} & \frac{1}{\mathrm{R}} & 0 \\ 0 & 0 & \frac{\mathrm{d}}{\mathrm{ds}} \end{bmatrix} \begin{Bmatrix} \mathrm{u} \\ \mathrm{v} \\ \varphi_z \end{Bmatrix} = \mathbf{B}(\mathrm{s})\mathbf{u} \tag{8}$$

where the matrix **B**(s) contains the derivative of the shape functions N(s) that reconstruct the element kinematic field by interpolating the nodal DOF $\mathrm{u^e}$ according to the equation:

$$\mathbf{u} = \mathbf{N}(\mathrm{s})\mathbf{u}^{\mathrm{e}} \tag{9}$$

Considering an infinitesimal curved segment subjected to distributed load p(s)ds, q(s)ds and m(s)ds (Fig. 3), the indefinite equilibrium equations relating to the tangent along the centroidal line, the radial direction and the rotation around the intersection point of the normal force axes, are:

$$\begin{aligned} \frac{\mathrm{dN}}{\mathrm{ds}} - \frac{\mathrm{T}}{\mathrm{R}} + \mathrm{p} &= 0 \\ \frac{\mathrm{dT}}{\mathrm{ds}} + \frac{\mathrm{N}}{\mathrm{R}} + \mathrm{q} &= 0 \\ \frac{\mathrm{dM}}{\mathrm{ds}} - \mathrm{T} + \mathrm{m} &= 0 \end{aligned} \tag{10}$$

where the curvilinear coordinate s is the independent variable, the normal force N, the shear force T and bending moment M are the unknown functions.

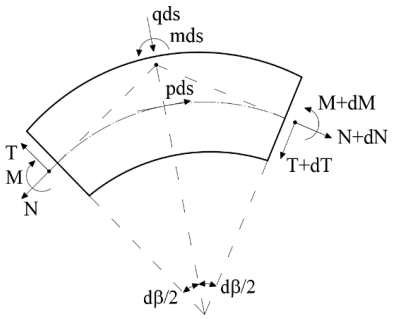

Fig. 3. Beam section force and moment.

3. Inverse Finite Element Method for Curved Beams

A brief description of the iFEM formulation is reported in this Section. To reconstruct the deformed shape of a discretized structure adopting the iFEM methodology, a least-squares functional, $\Phi(\mathbf{u})$, containing the difference between analytical and experimental section strains, need to be defined as (Tessler and Spangler [1, 2]):

$$\mathbf{\Phi}(\mathbf{u}) = \mathbf{e}(\mathbf{u}) - \mathbf{e}^{\varepsilon 2} \tag{11}$$

where $\mathbf{e}(\mathbf{u})$ contains the analytical strain field and $\mathbf{e}^{\varepsilon}$ is the experimental counterparts provided by strain sensors. For an individual curved element, the functional $\Phi(\mathbf{u})$ accounts the membrane-bending coupling according to Eq. 7 and is expressed by:

$$\mathbf{\Phi}_e(\mathbf{u}^e) = \boldsymbol{\varepsilon}_0(\mathbf{u}^e) - \boldsymbol{\varepsilon}_0^{\varepsilon 2} + \boldsymbol{\chi}_0(\mathbf{u}^e) - \boldsymbol{\chi}_0^{\varepsilon 2} \tag{12}$$

where the squared norms can be written in term of the normalized Euclidean norms

$$\begin{aligned} \boldsymbol{\varepsilon}_0(\mathbf{u}^e) - \boldsymbol{\varepsilon}_0^{\varepsilon 2} &= \frac{L^e}{n}\sum_{i=1}^{n}\left[\boldsymbol{\varepsilon}_0(s_i) - \boldsymbol{\varepsilon}_0^{\varepsilon}\right]^2 \\ \boldsymbol{\chi}_0(\mathbf{u}^e) - \boldsymbol{\chi}_0^{\varepsilon 2} &= \frac{I_z^e L^e}{A^e n}\sum_{i=1}^{n}\left[\boldsymbol{\chi}_0(s_i) - \boldsymbol{\chi}_0^{\varepsilon}\right]^2 \end{aligned} \tag{13}$$

for each of the n station points where the section strains are evaluated, located at the curvilinear coordinates s_i. Substituting Eq. 8 into Eq. 12, the inverse element matrix equation can be obtained by minimizing the functional $\Phi_e(\mathbf{u}^e)$ with respect to the nodal displacement, according to the original form of the iFEM framework:

$$\frac{d\mathbf{\Phi}_e(\mathbf{u}^e)}{d\mathbf{u}^e} = 0 \rightarrow \mathbf{K}^e\mathbf{u}^e = \mathbf{f}^e \tag{14}$$

where $\mathbf{K}^e$ and $\mathbf{f}^e$ can be explicitly written as:

$$\begin{aligned} \mathbf{K}^e &= \frac{L^e}{n}\sum_{i=1}^{n}\left[\mathbf{B}_{\varepsilon_0}^T(s_i)\mathbf{B}_{\varepsilon_0}(s_i)\right] + \frac{I_z^e L^e}{A^e n}\sum_{i=1}^{n}\left[\mathbf{B}_{\chi_0}^T(s_i)\mathbf{B}_{\chi_0}(s_i)\right] \\ \mathbf{f}^e &= \frac{L^e}{n}\sum_{i=1}^{n}\left[\mathbf{B}_{\varepsilon_0}^T(s_i)\varepsilon_{0,i}^{\varepsilon}\right] + \frac{I_z^e L^e}{A^e n}\sum_{i=1}^{n}\left[\mathbf{B}_{\chi_0}^T(s_i)\chi_{0,i}^{\varepsilon}\right] \end{aligned} \tag{15}$$

It can be highlighted that $\mathbf{K}^e$ should be computed once for a predefined locations of strain sensors, s_i, whereas $\mathbf{f}^e$ is a function of the measured strain values and needs to be updated at each strain data acquisition. Once the local matrices are established for individual inverse elements, their contributions can be assembled into the global resulting equation system of the discretized structure:

$$\mathbf{KU} = \mathbf{F} \tag{16}$$

after a proper transformation from the local to the global coordinate system. The matrix $\mathbf{K}$ is a singular matrix because it contains the rigid body motions. By imposing problem-dependent displacement boundary conditions, a solvable reduced system can be obtained:

$$\mathbf{K}_R\mathbf{U}_R = \mathbf{F}_R \tag{17}$$

where $\mathbf{K}_R$ is a positive definite matrix, $\mathbf{U}_R$ is the unknown DOF vector and $\mathbf{F}_R$ is the corresponding vector, dependent on the experimentally measured strains. The inverse of $\mathbf{K}_R$ that remains unchanged for a given distribution of strain sensors leads to the unknown DOF vector, $\mathbf{U}_R=\mathbf{K}_R^{-1}\mathbf{F}_R$, which provide the full-field displacements and strains throughout the inverse element domain. The evaluated strain components can be used within a constitutive relationship to predict stress distributions and enable failure criterion for a damage detection process. The last part of the iFEM formulation concerns the selection of shape functions suitable to represent the behavior of the structure considered.

4. New Curved Inverse Beam Elements iCB3, iCB4 and iCB5

The displacement parameters assumed to formulate the curved FE should satisfy the requirements of kinematic admissibility. Therefore, the radial and tangential displacement components together with the rotation should be continuous across the element boundaries. Furthermore, a FE suitable for general applications and having good convergence properties should include both strain-free and strain-inducing states. Considering the above requirements, highly efficient shape function can be derived by integrating the "exact" strain-displacement equations for the arbitrary curved beam reported in Eq. 7. Writing ε and χ in terms of strain functions $f_\varepsilon(\beta)$ and $f_\chi(\beta)$, the strain-displacement equations can be rewritten in a more general form as:

$$\frac{1}{R}\left(\frac{du}{d\beta} + v\right) = f_\varepsilon(\beta) \tag{18}$$

$$\frac{1}{R^2}\left(\frac{d^2v}{d\beta^2} - \frac{du}{d\beta}\right) = f_\chi(\beta) \tag{19}$$

Assuming $f_\varepsilon(\beta) = f_\chi(\beta) = 0$, it is equivalent to define the associated homogeneous equations corresponding to the zero-strain state. By substituting Eq. 18 into Eq. 19, and imposing the strain-free condition, the following system can be found:

$$\frac{du}{d\beta} + v = 0 \tag{20}$$

$$\frac{d^2v}{d\beta^2} + v = 0 \tag{21}$$

The solution of the associated homogeneous equations gives the displacements with zero strains, i.e. rigid-body displacements, which have the following form:

$$u = -a_1 \sin\beta + a_2 \cos\beta + a_3 \tag{22}$$

$$v = a_1 \cos\beta + a_2 \sin\beta \tag{23}$$

with a_1, a_2 and a_3 constants of integration. By developing the trigonometric function according to the Taylors' series, it can be obtained the uncoupled form given by Savino et al. [14]. Unlike this approximated solution, having the accuracy dependent by the order of the polynomial terms, the new rigid-body motions are exactly consistent with the strain-displacement equations. The general solution of the nonhomogeneous equations is the sum of the solution of the associated homogeneous equations and a particular solution of the nonhomogeneous equations depending by the functions $f_\varepsilon(\beta)$ and $f_\chi(\beta)$. A suitable choice of their degree must be made, to properly express the deformation of the element according to the number of DOF. On this assumption, three different two-node inverse elements have been developed with increasing accuracy named iCB3, iCB4 and iCB5.

Continuity across the nodes requires the specifications of the DOF at each end of the element. Since considering as nodal parameter approximated terms such as dv/ds instead of φ does not give the true generalized strain and stress, actual DOF have been selected starting by nine for the iCB3 element up to twelve for the iCB5 element:

$$\begin{aligned}
[\bar{w}]_{iCB3} &= [u_1\ v_1\ \varphi_1\ \chi_1\ u_2\ v_2\ \varphi_2\ \chi_2\ v_m] \\
[\bar{w}]_{iCB4} &= [u_1\ v_1\ \varphi_1\ \varepsilon_1\ \chi_1\ u_2\ v_2\ \varphi_2\ \varepsilon_2\ \chi_2] \\
[\bar{w}]_{iCB5} &= [u_1\ v_1\ \varphi_1\ \varepsilon_1\ \chi_1\ \chi_1'\ u_2\ v_2\ \varphi_2\ \varepsilon_2\ \chi_2\ \chi_2']
\end{aligned} \tag{24}$$

The initial nodal configuration of the iCB3 model is reduced to two nodes and eight DOF by applying the static condensation of the interior DOF (Fig. 4).

The resulting element has the reduced DOF vector:

$$[\bar{w}]_{iCB3} = [u_1\ v_1\ \varphi_1\ \chi_1\ u_2\ v_2\ \varphi_2\ \chi_2] \tag{25}$$

Considering that three of the aforementioned nodal parameters are required for the rigid-body displacements (Eq. 22, 23), the remaining available terms allow to define the independent constants of the following strain functions:

$$\begin{aligned}
f_{\varepsilon,\,iCB3} &= b_1 + b_2\beta + b_3\beta^2 \\
f_{\chi,\,iCB3} &= b_4 + b_5\beta + b_6\beta^2 \\
f_{\varepsilon,\,iCB4} &= b_1 + b_2\beta + b_3\beta^2 \\
f_{\chi,\,iCB4} &= b_4 + b_5\beta + b_6\beta^2 + b_7\beta^3 \\
f_{\varepsilon,\,iCB5} &= b_1 + b_2\beta + b_3\beta^2 + b_4\beta^3 \\
f_{\chi,\,iCB5} &= b_5 + b_6\beta + b_7\beta^2 + b_8\beta^3 + b_9\beta^4
\end{aligned} \tag{26}$$

Substituting each couple of strain functions in Eq. 18 and Eq. 19 for each type of inverse element, and by solving the nonhomogeneous differential equations, the particular solution can be obtained. For the sake of brevity, only the formulation of the iCB3 element is developed below; for the other elements the reader is referred to the Appendix.

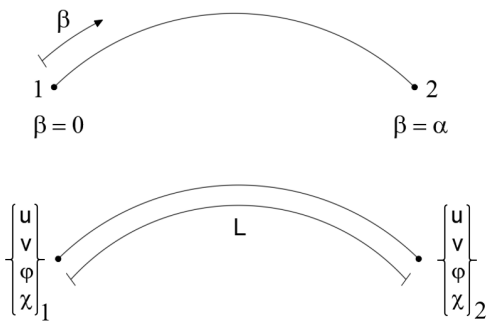

Fig. 4. iCB3 model.

Adding the solution of the homogeneous equations and the particular one, the general solution can be written as:

$$u_{iCB3}(\beta) = -a_1\sin\beta + a_2\cos\beta + a_3 - b_1R^2\beta - b_2\frac{R^2\beta^2}{2} + b_3\left(2R^2\beta - \frac{R^2\beta^3}{3}\right) + b_6 2R\beta$$
$$v_{iCB3}(\beta) = a_1\cos\beta + a_2\sin\beta + b_1R^2 + b_2R^2\beta + b_3\left(R^2\beta^2 - 2R^2\right) + b_4R + b_5R\beta + b_6\left(R\beta^2 - 2R\right) \tag{27}$$

where the terms a_1, a_2 and a_3 express the rigid-body displacements and the remaining coupled terms represent the deformation of the element. Once obtained the two unknowns u_{iCB3} and v_{iCB3}, all the other quantities can be derived by substituting Eq. 27 into Eq. 7. The generalized functions of the DOF can be expressed as follows:

$$[w] = [\beta][A] \tag{28}$$

where the terms are defined by:

$$[w]^T = \begin{bmatrix} u_{iCB3} & v_{iCB3} & \varphi_{iCB3} & \chi_{iCB3} \end{bmatrix}$$

$$[\beta] = \begin{bmatrix} -\sin\beta & \cos\beta & 1 & -R^2\beta & -\frac{R^2\beta^2}{2} & 2R^2\beta - \frac{R^2\beta^3}{3} & 0 & 0 & 2R\beta \\ \cos\beta & \sin\beta & 0 & R^2 & R^2\beta & R^2\beta^2 - 2R^2 & R & R\beta & R\beta^2 - 2R \\ 0 & 0 & -\frac{1}{R} & R\beta & R + \frac{R\beta^2}{2} & \frac{R\beta^3}{3} & 0 & 0 & R \\ 0 & 0 & 0 & 1 & \beta & \beta^2 & 0 & 0 & 0 \end{bmatrix}$$

$$[A]^T = \begin{bmatrix} a_1 & a_2 & a_3 & b_1 & b_2 & b_3 & b_4 & b_5 & b_6 \end{bmatrix}$$

The nodal conditions given by Eq. 26 can be written by the following:

$$[\bar{w}]_{iCB3} = [\bar{\beta}][A] \tag{29}$$

where:

$$[\bar{\beta}] = \begin{bmatrix} 0 & 1 & 1 & 0 & 0 & 0 & 0 & 0 & 0 \\ 1 & 0 & 0 & R^2 & 0 & -2R^2 & R & 0 & -2R \\ 0 & 0 & -\frac{1}{R} & 0 & R & 0 & 0 & 0 & R \\ 0 & 0 & 0 & 1 & 0 & 0 & 0 & 0 & 0 \\ -\sin\alpha & \cos\alpha & 1 & -R^2\alpha & -\frac{R^2\alpha^2}{2} & 2R^2\alpha - \frac{R^2\alpha^3}{3} & 0 & 0 & 2R\alpha \\ \cos\alpha & \sin\alpha & 0 & R^2 & R^2\alpha & R^2\alpha^2 - 2R^2 & R & R\alpha & R^2\alpha - 2R \\ 0 & 0 & -\frac{1}{R} & R\alpha & R + \frac{R\alpha^2}{2} & \frac{R\alpha^3}{3} & 0 & 0 & R \\ 0 & 0 & 0 & 1 & \alpha & \alpha^2 & 0 & 0 & 0 \\ \cos\frac{\alpha}{2} & \sin\frac{\alpha}{2} & 0 & R^2 & \frac{R^2\alpha}{2} & \frac{R^2\alpha^2}{4} - 2R^2 & R & \frac{R\alpha}{2} & \frac{R^2\alpha}{2} - 2R \end{bmatrix}$$

The next step involves the computation of the unknown coefficients following standard finite element procedures, after condensing the interior DOF. By inverting Eq. 29 and substituting the vector of unknown coefficient [A] in Eq. 28, yields to the final form:

$$[w] = [\beta][\bar{\beta}]^{-1}[\bar{w}] = [N][\bar{w}] \tag{30}$$

where [N] is the matrix of the shape functions. Note that the element shape functions are general enough to involve arbitrary applied loading, material properties and boundary conditions. The iFEM solution accuracy is dependent by the mesh refinement and the order of inverse element adopted. Finer shape functions would generally lead to more accurate results but require the availability of an increasing number of measured-strain data. According to the order of the strain functions given by Eq. 26, the singularity of the formulation is avoided if at least three, four and five station points are available for the elements iCB3, iCB4 and iCB5 respectively. Furthermore, considering the in-plane strain assumption adopted to define the experimental section strains from Eq. 6, at least two strain sensors are required for each station point. Therefore, the minimum number of strain sensors connected to the different order of the inverse elements is six, eight and ten for the iCB3, iCB4 and iCB5 element respectively.

Different numerical examples addressing the inverse elements accuracy and the number of station points required are presented in Section 5.

5. Numerical Simulation and Validation

Numerical examples of curved beams with rectangular cross section with different loading conditions are presented; the iFEM methodology is compared with the direct solutions of LUSAS Civil & Structural software which is a commercial finite element analysis program. The modelling of curved thin beams has been done using the BM3 Kirchhoff beam element, in which shear deformations are not included. The direct finite element analyses have been performed not only to numerically simulate the experimental measured strains in correspondence of the station points but also to establish the reference solution in terms of full displacements or section strains. Therefore, the simulated strain sensor data are then used as input to perform the iFEM analysis.

Finally, the accuracy of the iCB/iFEM formulation is assessed by the mean percentage difference (MPD) against the FEM reference solution, calculated as:

$$\mathrm{MPD}_g = \frac{1}{n}\sum_{i=1}^{n}\left(\frac{g_i^{iFEM} - g_i^{FEM}}{g_{max}^{FEM}}\right)100\% \tag{31}$$

where g_i indicates the value (strain or displacement) provided at the i-th location along each element, g_{max} is the corresponding maximum value considered as normalization factor and n is the total number of assessment nodes. The superscript "iFEM" refers to the reconstruction by iFEM while "FEM" refers to the simulated measurements.

5.1 Uniform circular beam

As a first example, the performance of the new inverse curved elements is demonstrated from the comparison with the independently interpolated model previously developed by Savino et al. [14]. The same curved beam with clamped-clamped boundary conditions has been considered (Fig. 5). The beam with rectangular cross section of height h = 0.5 m and base b = 0.3 m, radius of curvature R = 5 m and opening angle $\alpha = 180°$, is subjected to a static transverse distributed load of q = 1 KN/m. The beam is made of concrete having a Young's modulus of 30 GPa and Poisson's ratio of 0.2.

To establish an accurate reference solution, a mesh consisting of 20 elements and 140 DOF has been considered to perform the direct FEM analysis. To remain consistent with the work of Savino et al. [14], in the present iFEM analysis the same number of station points and locations are used throughout the curved beam axis (Fig. 6). This configuration is compatible with the minimum station points required by the iCB5 element, therefore the arch has been modelled considering an iCB5 with five station points.

In Fig. 7 the distribution along the arch of the displacements and strain obtained by the previous inverse curved beam element (Savino et al. [14]), the enhanced iCB5/iFEM formulation and the FEM analysis are compared. The iCB5/iFEM and direct FEM analyses produce the maximum transverse displacement v that differs by 0.02 %; it is 3.05 % in the case of the previous formulation. Improvements have been recorded also for strain readings. A prominent feature of these results is the disappearance of the oscillatory behaviour in the membrane strain distribution obtained using the previous formulation (Fig. 7c), (Savino et al. [14]).

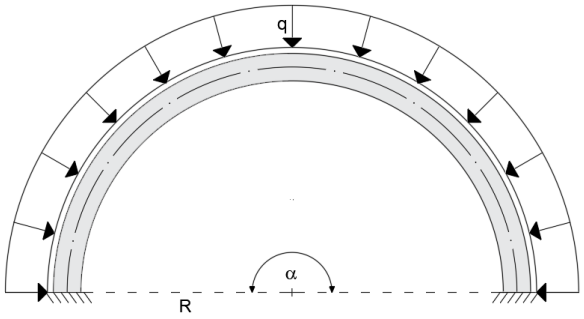

Fig. 5. Uniform circular beam under uniformly distributed load.

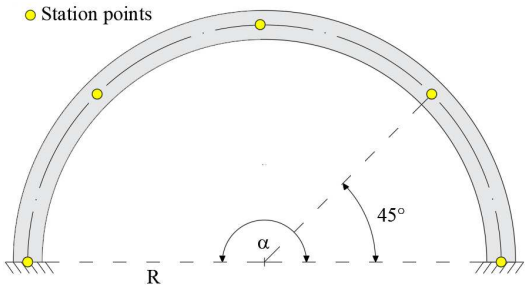

Fig. 6. Configuration of the iCB5 element.

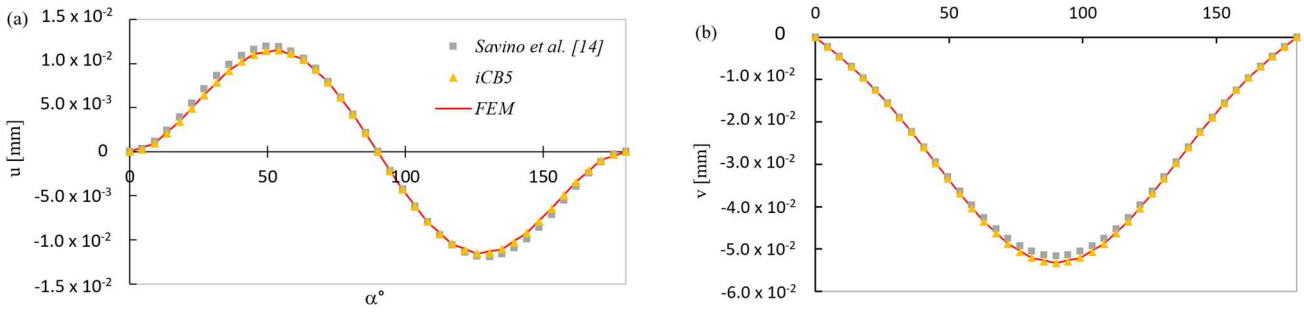

Fig. 7. Comparison along the arch axis of iFEM solution (Savino et al. [14], iCB5) to FEM analysis for the displacements u (a) and v (b), and strains ε (c) and χ (d).

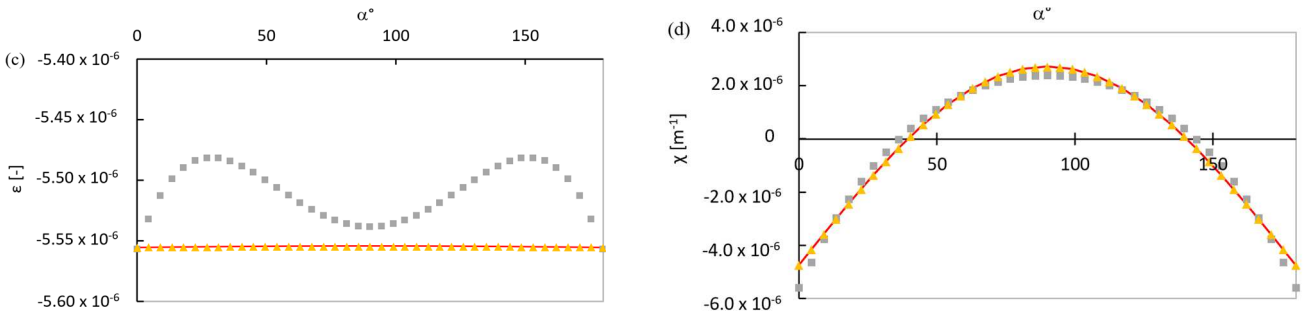

Fig. 7. Continued.

In Table 1, the accuracy metrics between the old iFEM formulation and the new iCB5 element are compared in terms of displacement and strain fields. In particular, a decrease in MPD is recorded for the iCB5 element both for displacements (MPD_u, MPD_v and MPD_ϕ) and strain (MPD_ε and MPD_χ), with the maximum MPD being less than 1%.

These results show the better shape sensing capability of the iCB5 element compared to Savino et al. [14] formulation, assuming the same configuration of station points.

5.2 Cantilever beam

To validate the bending and membrane response of iCB3, iCB4 and iCB5, a cantilever beam with a concentrated force F = 1 kN applied on the free end has been considered. Figure 8 shows the geometry of the curved beam having a radius of curvature R = 5 m, opening angle α = 90° and cross-section with height h = 0.5 m and base b = 0.3 m. The beam has an elastic modulus of the E = 30 GPa and Poisson's ratio of ν = 0.2.

To obtain an accurate reference solution by performing a direct FEM analysis, a refined mesh with 20 elements and 140 DOF is employed. This FEM analysis is also used to simulate the in-situ strain measurements. In comparison with the direct FEM analysis, the iFEM analyses are performed by using a coarse mesh with just one iCB3, iCB4 and iCB5 element respectively, with equally spaced strain sensors in a number of 3, 4 and 5 respectively (Fig. 9).

Figure 10 compares the distribution along the arch axis of the displacements u and v, calculated by means of the direct FEM analysis and the corresponding iCB3, iCB4 and iCB5 iFEM models.

Table 1. Mean-percent difference (MPD) for displacement and strain field corresponding to Savino et al. [14] and iCB5 models.

Model	MPD_u (%)	MPD_v (%)	MPD_ϕ (%)	MPD_ε (%)	MPD_χ (%)
Savino et al. [14]	3.14	0.90	4.05	0.79	5.48
iCB5	0.58	0.12	0.47	0.01	0.16

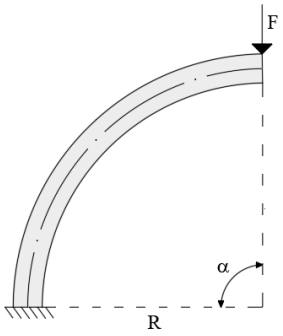

Fig. 8. Cantilever beam.

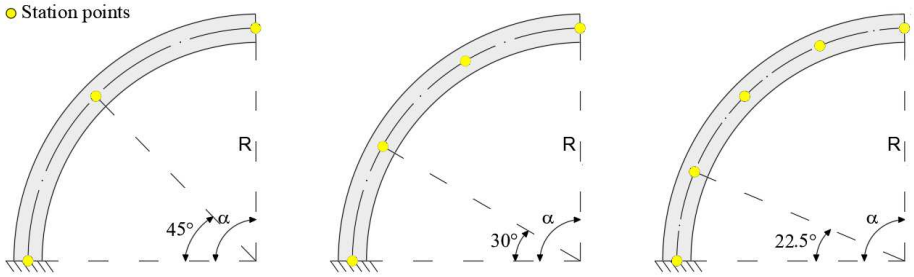

Fig. 9. Configuration of station points corresponding to iCB3, iCB4 and iCB5 model.

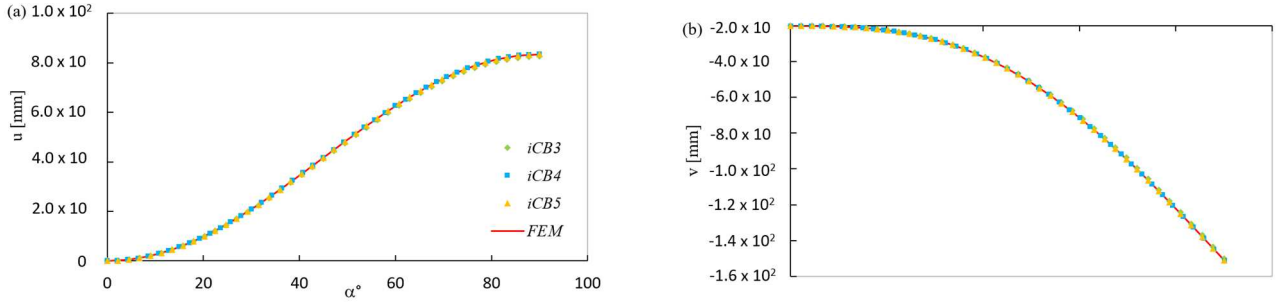

Fig. 10. Comparison along the arch axis of iFEM solution (iCB3, iCB4 and iCB5) to FEM displacements u (a) and v (b).

The global accuracy of each model is assessed considering the MPD between direct FEM solution and iFEM reconstructions for displacements and strain as listed in Table 2. According to the percentage differences in Table 2, the new models produce a maximum error of 1.32 % for displacements reconstructed by iCB3 model which further decreases using iCB5 element.

These results confirm the high performance of all the new inverse elements even for the least effective iCB3 element, which is on the other hand, the most useful for real SHM applications given the minimum number of strain sensors required

5.3 Influence of input data errors

To examine the predictive capabilities of the iCB/iFEM methodology for real engineering applications, it is convenient to assess the effect of data input errors on the solution accuracy. Therefore, the cantilever beam considered in the previous study is analyzed again using the input data coming from the direct FEM by adding an error of 1%, 5% and 10%, respectively (Fig. 8). Since the first station point is in common among the configurations of the three inverse elements (Fig. 9), it has been chosen as reference point to contain the simulated input strain measurement affected by error, according to the following equations:

$$\varepsilon_0(s_1)_{iFEM} = \varepsilon_0(s_1)_{FEM} + \text{err.} \times \varepsilon_0(s_1)_{FEM}$$

$$\chi_0(s_1)_{iFEM} = \chi_0(s_1)_{FEM} + \text{err.} \times \chi_0(s_1)_{FEM}$$

where $\varepsilon_0(s_1)_{FEM}$ and $\chi_0(s_1)_{FEM}$ are the tangential strain and curvature of the first station point simulated by the FEM analysis, err. represents the percentage error introduced above and $\varepsilon_0(s_1)_{iFEM}$ and $\chi_0(s_1)_{iFEM}$ are the input strains of the iFEM procedure. The accuracies of each model are assessed considering the MPD between iFEM and FEM results for displacements and strain field. In Tables 3-7, the MPD between iFEM and FEM predictions for the displacement and strain distributions are listed versus the percentage error introduced in the input strains of the first station point.

Table 2. Mean-percent differences (MPD) for displacement and strain field for iCB3, iCB4 and iCB5 iFEM models.

Model	MPD_u (%)	MPD_v (%)	MPD_ϕ (%)	MPD_ε (%)	MPD_χ (%)
iCB3	1.32	1.32	0.56	0.31	0.45
iCB4	1.13	0.12	0.11	0.04	0.11
iCB5	0.12	0.03	0.07	0.03	0.06

Table 3. Percent differences between the iFEM and FEM prediction for tangential displacement u.

Err. (%)	MPD_u (%)		
	iCB3	iCB4	iCB5
1	0.28	0.29	0.20
5	0.85	1.05	0.76
10	2.25	2.01	1.47

Table 4. Percent differences between the iFEM and FEM prediction for radial displacement v.

Err. (%)	MPD_v (%)		
	iCB3	iCB4	iCB5
1	0.17	0.11	0.07
5	0.37	0.43	0.29
10	1.03	0.85	0.59

Table 5. Percent differences between the iFEM and FEM prediction for rotation ϕ.

Err. (%)	MPD_ϕ (%)		
	iCB3	iCB4	iCB5
1	0.31	0.28	0.18
5	0.91	0.95	0.66
10	2.20	1.79	1.27

Table 6. Percent differences between the iFEM and FEM prediction for membrane strain ε.

Err. (%)	MPD_ε (%)		
	iCB3	iCB4	iCB5
1	1.15	1.01	0.27
5	1.17	1.09	0.91
10	1.92	1.73	1.71

Table 7. Percent differences between the iFEM and FEM prediction for curvature χ.

Err. (%)	MPD_χ (%)		
	iCB3	iCB4	iCB5
1	1.15	0.28	0.14
5	1.17	0.92	0.58
10	1.92	1.73	1.15

According to Tables 3-7, the percentage differences with the reference solutions result less than about 1% except in the cases with 10% of noise for iCB3 and iCB4 model, where it increases up to about 2%. These results confirm the higher performance of the iCB5 element compared to iCB3 and iCB4 element, especially in cases of input strain with high percentage error. However, satisfactory results are obtained even with the less powerful inverse elements, also considering the greater penalty induced when a lower number of station points is adopted.

Lastly, to examine the effects on the shape and strain sensing quality given by the availability of a quantity of station points higher than the minimum required, the previous example of uniform circular beam (Section 5.1) is revised considering a noise of 10 % on the first station point. More specifically, the performance of the iCB3 element considering three station points, five station points and a finer mesh with two iCB3 elements (Fig. 11) has been evaluated. Furthermore, a comparison with the metrics obtained using an iCB5 element with five station points is also reported. Therefore, the two elements can be compared considering the same penalty order on the total number of station points.

In Fig. 12, the displacements u and v obtained using the configuration specified above for the iCB3 element are compared to the direct FEM solution. In contrast to the static scheme (FEM results), it can be seen in the displacement distributions a slight asymmetry which is given by the error introduced in the first station point for the iFEM analyses.

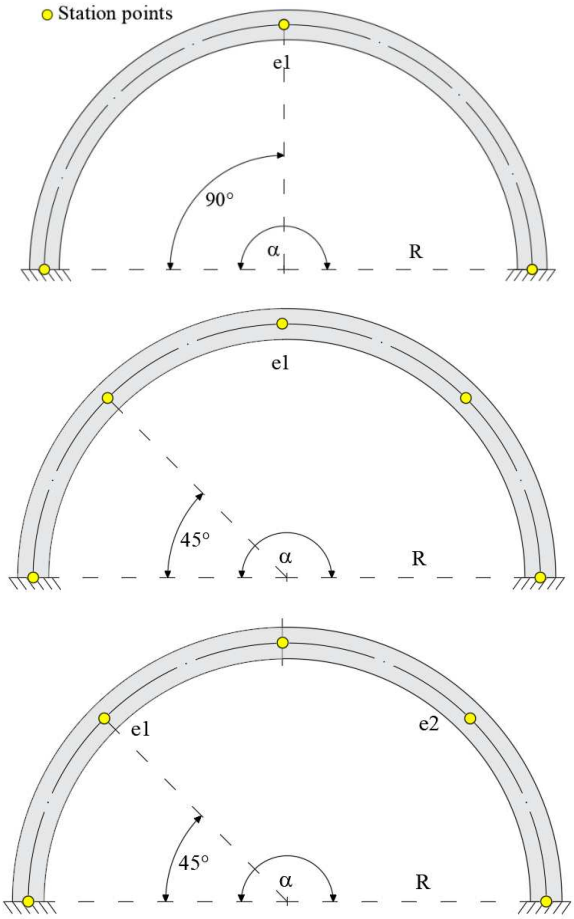

Fig. 11. Mesh configurations with iCB3.

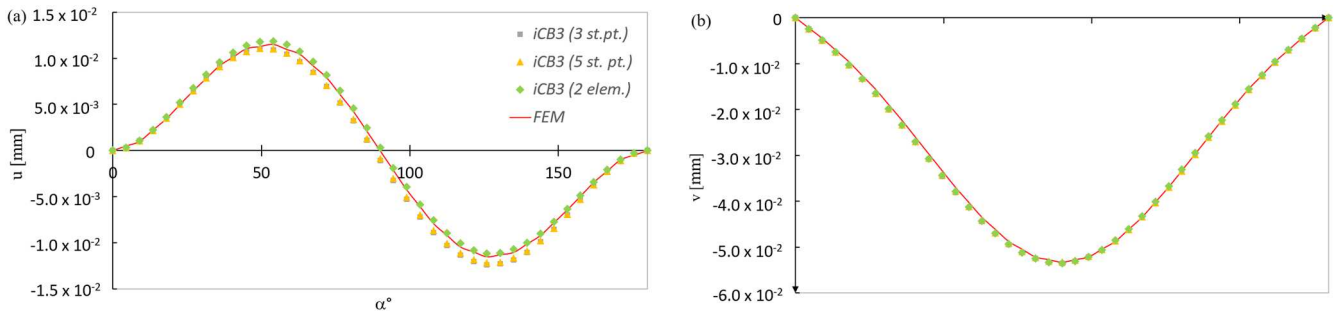

Fig. 12. Comparison of displacements u (a) and v (b) predicted by different iCB3 configurations and direct FEM solution.

Table 8. Mean-percent difference between iFEM (iCB3 (3 st.pt., 5 st.pt., 2 elem.), iCB5) and FEM predictions.

Model	MPD_u (%)	MPD_v (%)	MPD_ϕ (%)	MPD_ε (%)	MPD_χ (%)
iCB3 (3 st.pt.)	4.92	0.85	2.46	2.53	2.51
iCB3 (5 st.pt.)	3.99	0.65	2.16	2.20	2.51
iCB3 (2 elem.)	2.10	0.79	1.97	1.35	2.07
iCB5	1.77	0.80	1.74	1.60	1.76

As evident from Fig. 12, in case of a number of station points higher than the minimum required, it is better to adopt a finer mesh rather than consider the same inverse element with redundant station points. Thus, the error on the strain input data affects only a portion of the reconstructed deformed shape. To assess the global behavior of the three different configurations, the MPD has been computed in terms of both strains and displacements. Furthermore, a comparison with the MPD between iFEM and FEM predictions is reported in Table 8, considering also the outcomes obtained by modelling with an iCB5 element with five station points.

According to the MPD listed in Table 8, the iCB3 model shows a rapid reduction of the error passing from one element (iCB3 (3 st.pt.)) to two elements (iCB3 (2 elem.)), also considering few strain sensors and the high input data error introduced in the first station point. By comparing the MPDs obtained by modeling with one and two iCB3 elements on the same number of station points (2nd and 3rd row in Table 8), it can be seen the advantages of considering a finer mesh rather than modeling with a single element on a redundant number of station points. However, considering the model with iCB3 on five station points and the most powerful iCB5 element on the same number of station points, the MPD between iFEM and FEM results decreases and become less than 2 % with a single iCB5 element. Overall, these results prove the effectiveness of the improved iCB/iFEM formulation also in case of input data affected by error.

6. Conclusion

The inverse finite element method is a widely recognized procedure for the SHM in various engineering fields. Many inverse elements have been developed in the literature related to both one and two-dimensional geometry. Early formulation on curved inverse finite element was not enough effective due to the approximate solution of the strain-displacement relations. Much attention has been devoted in the present study to get an improved iFEM formulation to solve the inverse problem of shape and stress sensing of curved beam. The theoretical framework relies on the exact analytical solution of the strain-displacement differential equations and consequently involve the correct representation of the rigid-body displacements. Three different two-node curved beam models have been developed (iCB3, iCB4 and iCB5), each with an increasing order of accuracy according to the load configuration. One advantage of the present iFEM methodology is that accurate results can be obtained also when less powerful inverse elements are used; this is useful for practical applications where few strain sensors are available.

Numerical examples with different geometry and loading conditions were investigated. The results obtained were compared with reference solutions given by simulations performed with direct FEM analysis. Firstly, the superiority of the new formulation has been highlighted, by comparing the iCB5 element with the one present in the literature. Furthermore, the performance of the three inverse elements have been tested considering the same static scheme with the minimum required number of strain sensors. Finally, the robustness of the iCB/iFEM formulation was also verified, introducing errors on the input strain data. A good accuracy has been obtained even if the less powerful inverse curved element was adopted and therefore with the least number of strain sensors. Future work will concern the study of performance considering experimental tests in order to evaluate the influence of real strain sensors noise.

Author Contributions

P. Savino conceived of the present idea, developed the mathematical modeling and performed the computations. F. Tondolo planned the scheme, supervised and examined the theoretical validation of the manuscript. The manuscript was written through the contribution of all authors. All authors discussed the results, reviewed, and approved the final version of the manuscript.

Acknowledgments

Not Applicable.

Conflict of Interest

The authors declared no potential conflicts of interest concerning the research, authorship, and publication of this article.

Funding

The authors received no financial support for the research, authorship, and publication of this article.

Data Availability Statements

The datasets generated and/or analyzed during the current study are available from the corresponding author on reasonable request.

Nomenclature

A	Cross-section area	R	Radius of curvature [m]
a_i	Constants of integration associated with the i^{th} rigid-body motion	R_n	Radius at the neutral axis fiber
		r, β	Polar coordinate system
B(s)	Matrix of shape function derivatives	s, y, z	Local coordinate reference system
E	Young's modulus [GPa]	u	Tangential displacement [mm]
$\mathbf{e}^\varepsilon$	Experimental section strains	**u**	Vector of the kinematic variables
err.	Percentage error introduced in the simulated input strains [%]	$\mathbf{u}^e$	Vector of the nodal DOF
		$u_i(\beta), v_i(\beta)$	Numerical formulation of the displacement

e(u)	Vector of the section strains		field associated with the i^{th} inverse element
F	Global vector of the measured strains	u_s, u_r, u_z	Displacements along the s, y and z axes, respectively
F	Concentrated force [kN]		
f_ε	Function associated to the membrane strain	v	Radial displacement [mm]
f_χ	Function associated to the curvature	w	Vector of nodal parameters in terms of generalized functions
h, b	Height and base of the cross-section [m]		
Iz	Moment of inertia	$\overline{w}_i$	Vector of the nodal parameter associated with the i^{th} inverse element
K	Global matrix dependent from strain sensor locations	α	Opening angle [°]
L	Total length of the curved beam	ε_0	Tangential strain
MPD_g	Mean percentage difference of the g value [%]	ε_s	Normal strain in the cross-section
n	Number of station points	ν	Poisson's ratio
N(s)	Matrix of the shape functions	Φ	Least-squares functional
N, T, M	Normal force, shear force and bending moment	φ_z	Rotation about the z axis
p, q, m	Distributed load associated to the membrane, shear and bending component	χ_0	Curvature

Appendix

The development of the iCB models is based on the exact solutions of the strain-displacement differential equations and on the assumption of different degrees of interpolation. Consequently, three models have been developed (iCB3, iCB4 and iCB5) having nine, ten and twelve nodal parameters, respectively. This section describes the equations and the matrix related to the development of the iCB4 and iCB5 elements.

For iCB4 element, the solution of the differential equations gives the following equations:

$$\begin{aligned} u_{iCB4}(\beta) &= -a_1\sin\beta + a_2\cos\beta + a_3 + b_3 2R\beta - b_4R^2\beta - b_5\frac{R^2\beta^2}{2} + b_6\left(2R^2\beta - \frac{R^2\beta^3}{3}\right) + b_7\left(3R^2\beta^2 - \frac{R^2\beta^4}{4}\right) \\ v_{iCB4}(\beta) &= a_1\cos\beta + a_2\sin\beta + b_1R + b_2R\beta + b_3\left(R\beta^2 - 2R\right) + b_4R^2 + b_5R^2\beta + b_6\left(R^2\beta^2 - 2R^2\right) + b_7\left(R^2\beta^3 - 6R^2\beta\right) \end{aligned} \tag{A.1}$$

where the unknown coefficients can be obtained considering the following DOF of the element:

$$[w]^T = \left[u_{iCB4} \quad v_{iCB4} \quad \varphi_{iCB4} \quad \varepsilon_{iCB4} \quad \chi_{iCB4}\right] \tag{A.2}$$

Assuming the kinematics equations of the curved beam, the vector [w] can be explained in the matrix form:

$$[w] = [\beta][A] \tag{A.3}$$

where:

$$[\beta] = \begin{bmatrix} -\sin\beta & \cos\beta & 1 & 0 & 0 & 2R\beta & -R^2\beta & -\frac{R^2\beta^2}{2} & 2R^2\beta - \frac{R^2\beta^3}{3} & 3R^2\beta^2 - \frac{R^2\beta^4}{4} \\ \cos\beta & \sin\beta & 0 & R & R\beta & R\beta^2 - 2R & R^2 & R^2\beta & R^2\beta^2 - 2R^2 & R^2\beta^3 - 6R^2\beta \\ 0 & 0 & -\frac{1}{R} & 0 & 1 & 0 & R\beta & R + \frac{R\beta^2}{2} & \frac{R\beta^3}{3} & \frac{R\beta^4}{4} - 6R \\ 0 & 0 & 0 & 1 & \beta & \beta^2 & 0 & 0 & 0 & 0 \\ 0 & 0 & 0 & 0 & 0 & 0 & 1 & \beta & \beta^2 & \beta^3 \end{bmatrix} \tag{A.4}$$

$$[A]^T = \left[a_1 \quad a_2 \quad a_3 \quad b_1 \quad b_2 \quad b_3 \quad b_4 \quad b_5 \quad b_6 \quad b_7\right] \tag{A.5}$$

By imposing the continuity of each DOF, the matrix that allows to define the unknown coefficients results:

$$[\overline{\beta}] = \begin{bmatrix} 0 & 1 & 1 & 0 & 0 & 0 & 0 & 0 & 0 & 0 \\ 1 & 0 & 0 & R & 0 & -2R & R^2 & 0 & -2R^2 & 0 \\ 0 & 0 & -\frac{1}{R} & 0 & 1 & 0 & 0 & R & 0 & -6R \\ 0 & 0 & 0 & 1 & 0 & 0 & 0 & 0 & 0 & 0 \\ 0 & 0 & 0 & 0 & 0 & 0 & 1 & 0 & 0 & 0 \\ -\sin\alpha & \cos\alpha & 1 & 0 & 0 & 2R\alpha & -R^2\alpha & \frac{-R^2\alpha^2}{2} & 2R^2\alpha - \frac{R^2\alpha^3}{3} & 3R^2\alpha^2 - \frac{R^2\alpha^4}{4} \\ \cos\alpha & \sin\alpha & 0 & R & R\alpha & R\alpha^2 - 2R & R^2 & R^2\alpha & R^2\alpha^2 - 2R^2 & R^2\alpha^3 - 6R^2\alpha \\ 0 & 0 & -\frac{1}{R} & 0 & 1 & 0 & R\alpha & R + \frac{R\alpha^2}{2} & \frac{R\alpha^3}{3} & \frac{R\alpha^4}{4} - 6R \\ 0 & 0 & 0 & 1 & \alpha & \alpha^2 & 0 & 0 & 0 & 0 \\ 0 & 0 & 0 & 0 & 0 & 0 & 1 & \alpha & \alpha^2 & \alpha^3 \end{bmatrix} \tag{A.6}$$

The solution of the system provides the vector [A] which allows to express the functions [w] in terms of nodal parameters. Considering the same procedure also for the iCB5 element, the displacements vary over the element length as:

$$u_{iCB5}(\beta) = -a_1\sin\beta + a_2\cos\beta + a_3 + b_3 2R\beta + b_4 3R\beta^2 - b_5 R^2\beta - b_6\frac{R^2\beta^2}{2} + b_7\left(2R^2\beta - \frac{R^2\beta^3}{3}\right) + b_8\left(3R^2\beta^2 - \frac{R^2\beta^4}{4}\right) + b_9\left(4R^2\beta^3 - 24R^2\beta - \frac{R^2\beta^5}{5}\right) \tag{A.7}$$

$$v_{iCB5}(\beta) = a_1\cos\beta + c_2\sin\beta + b_1 R + b_2 R\beta + b_3\left(R\beta^2 - 2R\right) + b_4\left(R\beta^3 - 6R\beta\right) + b_5 R^2 + b_6 R^2\beta + b_7\left(R^2\beta^2 - 2R^2\right) + b_8\left(R^2\beta^3 - 6R^2\beta\right) + b_9\left(24R^2 - 12R^2\beta^2 + R^2\beta^4\right) \tag{A.8}$$

The consequent variables considered to develop the shape functions that approximate both membrane and bending deformations of the iCB5 element are:

$$[w]^T = \left[u_{iCB5} \quad v_{iCB5} \quad \varphi_{iCB5} \quad \varepsilon_{iCB5} \quad \chi_{iCB5} \quad \chi'_{iCB5}\right] \tag{A.9}$$

which are defined in matrix notation by:

$$[\beta] = \begin{bmatrix} -\sin\beta & \cos\beta & 1 & 0 & 0 & 2R\beta & 3R\beta^2 & -R^2\beta & -\frac{R^2\beta^2}{2} & 2R^2\beta - \frac{R^2\beta^3}{3} & 3R^2\beta^2 - \frac{R^2\beta^4}{4} & 4R^2\beta^3 - 24R^2\beta - \frac{R^2\beta^5}{5} \\ \cos\beta & \sin\beta & 0 & R & R\beta & R\beta^2 - 2R & R\beta^3 - 6R\beta & R^2 & R^2\beta & R^2\beta^2 - 2R^2 & R^2\beta^3 - 6R^2\beta & 24R^2 - 12R^2\beta^2 + R^2\beta^4 \\ 0 & 0 & -\frac{1}{R} & 0 & 1 & 0 & -6 & R\beta & R + \frac{R\beta^2}{2} & \frac{R\beta^3}{3} & \frac{R\beta^4}{4} - 6R & \frac{R\beta^5}{5} \\ 0 & 0 & 0 & 1 & \beta & \beta^2 & \beta^3 & 0 & 0 & 0 & 0 & 0 \\ 0 & 0 & 0 & 0 & 0 & 0 & 0 & 1 & \beta & \beta^2 & \beta^3 & \beta^4 \\ 0 & 0 & 0 & 0 & 0 & 0 & 0 & 0 & 1 & 2\beta & 3\beta^2 & 4\beta^3 \end{bmatrix} \tag{A.10}$$

$$[A]^T = \left[a_1 \quad a_2 \quad a_3 \quad b_1 \quad b_2 \quad b_3 \quad b_4 \quad b_5 \quad b_6 \quad b_7 \quad b_8 \quad b_9\right]$$

The matrix referred to the imposition of the nodal conditions is:

$$[\bar{\beta}] = \begin{bmatrix} 0 & 1 & 1 & 0 & 0 & 0 & 0 & 0 & 0 & 0 & 0 & 0 \\ 1 & 0 & 0 & R & 0 & -2R & 0 & R^2 & 0 & -2R^2 & 0 & 24R^2 \\ 0 & 0 & -\frac{1}{R} & 0 & 1 & 0 & -6 & 0 & R & 0 & -6R & 0 \\ 0 & 0 & 0 & 1 & 0 & 0 & 0 & 0 & 0 & 0 & 0 & 0 \\ 0 & 0 & 0 & 0 & 0 & 0 & 0 & 1 & 0 & 0 & 0 & 0 \\ 0 & 0 & 0 & 0 & 0 & 0 & 0 & 0 & 1 & 0 & 0 & 0 \\ -\sin\alpha & \cos\alpha & 1 & 0 & 0 & 2R\alpha & 3R\alpha^2 & -R^2\alpha & -\frac{R^2\alpha^2}{2} & 2R^2\alpha - \frac{R^2\alpha^3}{3} & 3R^2\alpha^2 - \frac{R^2\alpha^4}{4} & 4R^2\alpha^3 - 24R^2\alpha - \frac{R^2\alpha^5}{5} \\ \cos\alpha & \sin\alpha & 0 & R & R\alpha & R\alpha^2 - 2R & R\alpha^3 - 6R\alpha & R^2 & R^2\alpha & R^2\alpha^2 - 2R^2 & R^2\alpha^3 - 6R^2\alpha & 24R^2 - 12R^2\alpha^2 + R^2\alpha^4 \\ 0 & 0 & -\frac{1}{R} & 0 & 1 & 0 & -6 & R\alpha & R + \frac{R\alpha^2}{2} & \frac{R\alpha^3}{3} & \frac{R\alpha^4}{4} - 6R & \frac{R\alpha^5}{5} \\ 0 & 0 & 0 & 1 & \alpha & \alpha^2 & \alpha^3 & 0 & 0 & 0 & 0 & 0 \\ 0 & 0 & 0 & 0 & 0 & 0 & 0 & 1 & \alpha & \alpha^2 & \alpha^3 & \alpha^4 \\ 0 & 0 & 0 & 0 & 0 & 0 & 0 & 0 & 1 & 2\alpha & 3\alpha^2 & 4\alpha^3 \end{bmatrix} \tag{A.11}$$

References

[1] Tessler, A., Spangler, J.L., A Variational Principle for Reconstruction of Elastic Deformations in Shear Deformable Plates and Shells, *NASA/TM-2003-212445*, 2003.

[2] Tessler, A., Spangler, J.L., A least-squares variational method for full-field reconstruction of elastic deformations in shear-deformable plates and shells, *Computer Methods in Applied Mechanics and Engineering*, 194(2-5), 2005, 327-339.

[3] Gherlone, M., Beam inverse finite element formulation, *LAQ Rep. Politecnico di Torino*, 2008.

[4] Gherlone, M., Cerracchio, P., Mattone, M., Di Sciuva, M., Tessler, A., Dynamic shape reconstruction of three-dimensional frame structures using the inverse finite element method, *Proceedings of 3rd ECCOMAS Thematic Conference on Computational Methods in Structural Dynamics and Earthquake Engineering*, Corfù, Greece, 2011.

[5] Gherlone, M., Cerracchio, P., Mattone, M., Di Sciuva, M., Tessler, A., Shape Sensing of 3D frame structures using an inverse Finite Element Method, *International Journal of Solids and Structures*, 49, 2012, 3100-3112.

[6] Cerracchio, P., Gherlone, M., Di Sciuva, M., Tessler, A., A novel approach for displacement and stress monitoring of sandwich structures based on the inverse Finite Element Method, *Composite Structures*, 127, 2015, 69-76.

[7] Kefal, A., Oterkus, E., Tessler, A., Spangler, J.L., A quadrilateral inverse-shell element with drilling degrees of freedom for shape sensing and structural health monitoring, *Engineering Science and Technology, an International Journal*, 19, 2016, 1299-1313.

[8] Kefal, A., Tessler, A., Oterkus, E., An enhanced inverse finite element method for displacement and stress monitoring of multilayered composite and sandwich structures, *Composite Structures*, 179, 2017, 514-540.

[9] Tessler, A., Roy, R., Esposito, E., Surace, C., Gherlone, M., Shape Sensing of Plate and Shell Structures Undergoing Large Displacements Using the Inverse Finite Element Method, *Shock and Vibration*, 2018, 2018, 8076085.

[10] Kefal, A., An efficient curved inverse-shell element for shape sensing and structural health monitoring of cylindrical marine structures, *Ocean Engineering*, 188, 2019, 106262.

[11] Savino, P., Gherlone, M., Tondolo, F., Shape sensing with inverse finite element method for slender structures, *Structural Engineering & Mechanics*, 72(2), 2019, 217-227.

[12] Kefal, A., Tabrizi, I.E., Yildiz, M., Tessler, A., A smoothed iFEM approach for efficient shape-sensing applications: Numerical and experimental validation on composite structures, *Mechanical Systems and Signal Processing*, 152, 2021, 107486.

[13] Kefal, A., Oterkus, E., Isogeometric iFEM Analysis of Thin Shell Structures, *Sensors*, 20(9), 2020, 2685.

[14] Savino, P., Tondolo, F., Gherlone, M., Tessler, A., Application of Inverse Finite Element Method to Shape Sensing of Curved Beams, *Sensors*, 20(24), 2020, 7012.

[15] Colombo, L., Sbarufatti, C., Giglio, M., Definition of a load adaptive baseline by inverse finite element method for structural damage identification, *Mechanical Systems and Signal Processing*, 120, 2019, 584-607.

[16] Colombo, L., Oboe, D., Sbarufatti, C., Cadini, F., Russo, S., Giglio, M., Shape sensing and damage identification with iFEM on a composite structure subjected to impact damage and non-trivial boundary conditions, *Mechanical Systems and Signal Processing*, 148, 2021, 107163.

[17] Roy, R., Gherlone, M., Surace, C., Damage Localisation in Thin Plates Using the Inverse Finite Element Method, *Proceedings of the 13th International Conference on Damage Assessment of Structures. Lecture Notes in Mechanical Engineering*, Springer, Singapore, 2020.
[18] Li, M., Kefal, A., Cerik, B.C., Oterkus, E., Dent damage identification in stiffened cylindrical structures using inverse Finite Element Method, *Ocean Engineering*, 198, 2020, 106944.
[19] Oboe, D., Colombo, L., Sbarufatti, C., Giglio, M., Comparison of strain pre-extrapolation techniques for shape and strain sensing by iFEM of a composite plate subjected to compression buckling, *Composite Structures*, 262, 2021, 113587.
[20] Quach, C.C., Vazquez, S.L., Tessler, A., Moore, J.P., Cooper, E.G., Structural Anomaly Detection Using Fiber Optic Sensors and Inverse Finite Element Method, *AIAA Guidance, Navigation, and Control Conference and Exhibit*, San Francisco, California, 2005.
[21] Gherlone, M., Cerracchio, P., Mattone, M., Di Sciuva, M., Tessler, A., Beam shape sensing using inverse finite element method: theory and experimental validation, *Proceeding of 8th International Workshop on Structural Health Monitoring*, Stanford, California, 2011.
[22] Gherlone, M., Cerracchio, P., Mattone, M., Di Sciuva, M., Tessler, A., An inverse finite element method for beam shape sensing: theoretical framework and experimental validation, *Smart Material and Structures*, 23(4), 2014, 045027.
[23] Kefal, A., Oterkus, E., Displacement and stress monitoring of a chemical tanker based on inverse finite element method, *Ocean Engineering*, 112, 2016, 33-46.
[24] Kefal, A., Oterkus, E., Displacement and stress monitoring of a Panamax containership using inverse finite element method, *Ocean Engineering*, 119, 2016, 16-29.
[25] Papa, U., Russo S., Lamboglia, A., Del Core, G., Iannuzzo, G., Health structure monitoring for the design of an innovative UAS fixed wing through inverse finite element method (iFEM), *Aerospace Science and Technology*, 69, 2017, 439-448.
[26] Kefal, A., Yildiz, M., Modeling of Sensor Placement Strategy for Shape Sensing and Structural Health Monitoring of a Wing-Shaped Sandwich Panel Using Inverse Finite Element Method, *Sensors*, 17(12), 2017, 2775.
[27] Zhao, Y., Bao, H., Duan, X., Fang, H., The Application Research of Inverse Finite Element Method for Frame Deformation Estimation, *International Journal of Aerospace Engineering*, 2017, 2017, 1326309.
[28] Liu, M., Zhang, X., Song, H., Zhou, S., Zhou, Z., Zhou, W., Inverse Finite Element Method for Reconstruction of Deformation in the Gantry Structure of Heavy-Duty Machine Tool Using FBG Sensors, *Sensors*, 18(7), 2018, 2173.
[29] Liu, M., Zhang, X., Song, H., Wang, J., Zhou, S., Reconstruction algorithm for obtaining the bending deformation of the base of heavy-duty machine tool using inverse finite element method, *Metrology and Measurement System*, 25(4), 2018, 727-741.
[30] Liu, M., Zhou, F., Song, H., Yang, X., Wang, J., Deformation Reconstruction for a Heavy-Duty Machine Column Through the Inverse Finite Element Method, *IEEE Sensors Journal*, 20(16), 2020, 9218-9225.
[31] Zhao, Y., Du, J., Bao, H., Xu, Q., Optimal Sensor Placement Based on Eigenvalues Analysis for Sensing Deformation of Wing Frame Using iFEM, *Sensors*, 18(8), 2018, 2424.
[32] Zhao, Y., Du, J., Bao, H., Xu, Q., Optimal Sensor Placement for Inverse Finite Element Reconstruction of Three-Dimensional Frame Deformation, *International Journal of Aerospace Engineering*, 2018, 2018, 6121293.
[33] Kobayashi, M., Murayama, H., Shape sensing for pipe structures by inverse finite element method based on distributed fiber-optic sensors, *26th International Conference on Optical Fiber Sensors*, Lausanne, Switzerland, 2018.
[34] Kefal, A., Mayang, J.B., Oterkus, E., Yildiz, M., Three dimensional shape and stress monitoring of bulk carriers based on iFEM methodology, *Ocean Engineering*, 147, 2018, 256-267.
[35] Niu, S., Li, K., Liu, J., Bao, H., A Refined Shape Sensing Method for Skin Antenna Structure Based on Inverse Finite Element Method, *Applied Sciences*, 10(21), 2020, 7620.
[36] Li, M., Kefal, A., Oterkus, E., Oterkus, S., Structural health monitoring of an offshore wind turbine tower using iFEM methodology, *Ocean Engineering*, 204. 2020, 107291.
[37] Dawe, D.J., Rigid-body motions and strain-displacement equations of curved shell finite elements, *International Journal of Mechanical Sciences*, 14(9), 1972, 569-578.
[38] Dawe, D.J., Curved finite elements for the analysis of shallow and deep arches, *Computers & Structures*, 4(3), 1974, 559-580.
[39] FEA Ltd, *LUSAS Finite Element System V15.1: User's Manual*, FEA Ltd, UK, 1995.
[40] Qatu, M.S., Theories and analyses of thin and moderately thick laminated composite curved beams, *International Journal of Solids and Structures*, 30(20), 1993, 2743-2756.

ORCID iD

Pierclaudio Savino https://orcid.org/0000-0001-8945-4030
Francesco Tondolo https://orcid.org/0000-0003-0258-3054

How to cite this article: Savino P., Tondolo F. Two-node Curved Inverse Finite Element Formulations based on Exact Strain-displacement Solution, *J. Appl. Comput. Mech.*, xx(x), 2023, 1–15. https://doi.org/10.22055/jacm.2022.41150.3708